First- and Higher-Order Correlation Detection Using Wavelet Transforms

K. Gurley, M.ASCE[1]; T. Kijewski, S.M.ASCE[2]; and A. Kareem, M.ASCE[3]

Abstract: In order to detect intermittent first- and higher-order correlation between a pair of signals in both time and frequency, a wavelet-based coherence and bicoherence technique was developed. Due to the limited averaging in a time-frequency coherence estimate, spurious correlated pockets were detected due to statistical variance. The introduction of multiresolution, localized integration windows was shown to minimize this effect. A coarse ridge extraction scheme utilizing hard thresholding was then applied to extract meaningful coherence. This thresholding scheme was further enhanced through the use of "smart" thresholding maps, which represent the likely statistical noise between uncorrelated simulated signals bearing the same power spectral density and probability-density function as the measured signals. It was demonstrated that the resulting filtered wavelet coherence and bicoherence maps were capable of capturing low levels of first- and higher-order correlation over short time spans despite the presence of ubiquitous leakage and variance errors. Immediate applications of these correlation detection analysis schemes can be found in the areas of bluff body aerodynamics, wave-structure interactions, and seismic response of structures where intermittent correlation between linear and nonlinear processes is of interest.

Introduction

Though transients have long defined signature characteristics across the engineering spectrum, available analysis tools like Fourier transforms have been ill equipped to represent this phenomenon. It was not until the time-frequency revolution of the 20th century that such signals could be adequately treated by the likes of the Gabor transform and the Wigner-Ville distribution. Today, wavelet transforms lead the transition to this new analysis domain, providing the ability to display time and frequency information independently and unveil the hidden features of evolutionary phenomena.

Particularly in the areas of aerodynamics and wind engineering, wind field fluctuations result in spatiotemporal pressure fluctuations on the surfaces of bluff bodies, e.g., buildings. These pressure fluctuations are manifestations of complex, nonlinear interactions that take place as the wind passes around a bluff structure. The spatiotemporal pressure fluctuations exhibit drastic transient features depending on their location on the surface and, with the exception of the windward face, are not amenable to a functional relationship with the oncoming wind field. Efforts to identify significant linear correlation between wind and pressure fluctuations were unsuccessful, especially in the separated flow regions. This has led to the consideration of higher-order correlation, e.g., bicoherence (Gurley et al. 1997). However, these efforts highlighted the inability of such Fourier-based measures to capture transient higher-order correlations that may exist between wind and pressure fluctuations.

With the availability of time-frequency analysis via wavelets, linear correlation analyses were enhanced by way of the coscalogram (Gurley and Kareem 1999a). This approach did identify some intermittent correlation between wind and pressure and will be further developed in this study as a tool for delineating any previously obscured intermittent relationship between certain wavelengths in the approach flow and the resulting pressure fluctuations. The potential for such insights have lent wavelets to other applications in wind engineering. For example, early investigations of turbulent wind effects were conducted by Farge (1992), who applied wavelet-based spectral analysis to the modeling of atmospheric turbulence. Gurley and Kareem (1997a) later adapted this to the analysis of turbulence and resulting pressures in full-scale dynamic response data. In total, the use of wavelet transforms in this field continues to advance, as overviewed by Gurley and Kareem (1999a) in their study showcasing applications of wavelets in wind, offshore, and earthquake engineering.

Unfortunately, though the wavelet coscalogram was successful in identifying intermittent linear correlation between wind speed and pressure, it failed to reveal the instantaneous higher-order correlations that may exist in the transient spikes of fluctuating pressures. While Fourier-based higher-order spectral measures such as bicoherence can capture higher-order correlations, they have difficulty detecting such intermittent nonlinear interactions. The same can be said for the case of high amplitude, nonlinear extreme waves, whose first- and second-order components are

[1]Assistant Professor, Dept. of Civil and Coastal Engineering, Univ. of Florida, P.O. Box 116580, Gainesville, FL 32611-6580. E-mail: kgurl@ce.ufl.edu

[2]Graduate Student, NatHaz Modeling Laboratory, Dept. of Civil Engineering and Geological Sciences, Univ. of Notre Dame, 156 Fitzpatrick Hall, Notre Dame, IN 46556-0767. E-mail: tkijewsk@nd.edu

[3]Professor and Chair, Dept. of Civil Engineering and Geological Sciences, Univ. of Notre Dame, 156 Fitzpatrick Hall, Notre Dame, IN 46556-0767. E-mail: kareem@nd.edu

phase coupled over relatively short intervals (Powers et al. 1997). This motivated the need for wavelet-based measures such as bicoherence to study nonstationary and nonlinear characteristics of random waves and the resulting response of floating offshore platforms, as well as prompting their consideration in this study for higher-order intermittent correlation analysis of wind velocity and fluctuating pressures.

This study continues the work in wavelets for both wind and waves by applying wavelet transforms to identify first- and higher-order intermittent correlation between measured records. While this representation allows a display in terms of time and frequency, the influence of noise in the estimation of coherence and bicoherence over a localized time frame is significant, making a distinction between the true correlation and noise a major issue to be addressed. This study revisits the classical approach for reduction of variance, averaging, in the multiresolution context of wavelets, and later discusses denoising schemes, which minimize the need for localized averaging in order to preserve temporal information. While hard thresholding based on global maxima of the wavelet coherence map can be used to isolate meaningful coherence, a "smart" thresholding simulation scheme is proposed to provide a reference noise map to more accurately separate spurious noise effects from true signal content. This reference map is generated using independent realizations of time histories that match the power spectrum and probability contents of the signals being analyzed to establish a statistical measure of the expected noise in the estimated coherence and bicoherence. Though relatively intensive, this scheme's robustness is established using both simulated and measured data. The method is shown to significantly reduce the presence of spurious coherence, even in cases where variance and leakage are prevalent. The performance of these techniques is then validated by example in the case of both wind-pressure effects on bluff bodies and offshore platform surge response.

Wavelet Transform Background

Wavelet analysis (Daubechies 1988; Strang and Nguyen 1996) decomposes a signal via a set of finite basis functions, revealing transient characteristics obscured by the trigonometric basis functions used in Fourier analysis. Wavelet coefficients $W_x(a,t)$ are produced through the convolution of a scaled parent wavelet function $\psi(t)$ with the analyzed signal $x(t)$

$$W_x(a,t) = \frac{1}{\sqrt{|a|}} \int_{-\infty}^{\infty} x(\tau)\psi\left(\frac{t-\tau}{a}\right) d\tau \qquad (1)$$

where a = scale of the wavelet, inversely proportional to frequency and t = local time origin of the analyzing wavelet.

As harmonic analysis is quite intuitive, the results of this study are interpreted in the time-frequency domain, rather than the time-scale domain natural to the wavelet transform. This perspective is facilitated by choosing the Morlet wavelet (Grossman and Morlet 1985) as the parent wavelet, with its well-defined relationship between scale and frequency

$$\psi(t) = e^{-t^2/2}e^{j2\pi f_o t} = e^{-t^2/2}[\cos(2\pi f_o t) + j\sin(2\pi f_o t)] \qquad (2a)$$

$$f \cong \frac{f_o}{a} \qquad (2b)$$

As shown in Kijewski and Kareem (2002a), the parameter f_o, the wavelet's central frequency, dictates the time and frequency resolutions of the wavelet analysis and should always be adjusted accordingly. The resulting variable time Δt and frequency Δf resolutions are merely scaled versions of the duration and bandwidth of the Gaussian window in Eq. (2a), as determined by Gabor's (1946) mean square definition, and later given by Chui (1992) as

$$\Delta t = \frac{a}{\sqrt{2}} \qquad (3a)$$

$$\Delta f = \frac{1}{a 2\pi\sqrt{2}} \qquad (3b)$$

Though a considerable amount of work in wavelet transform theory has been assembled, for a host of parent wavelets, extensive development of these topics could not be included in this paper, for the sake of brevity. As a result, only relationships directly relevant to the discussions herein are provided via Eqs. (1)–(3). A more detailed discussion of wavelet transforms and associated theorems may be found in a number of textbooks, including Daubechies (1992); Burrus et al. (1998); Carmona et al. (1998); and Mallat (1998).

Wavelet Coherence Background-Scalogram and Coscalogram

The localized wavelet coefficients are well suited for analyzing nonstationary events, with their squared values plotted on a time-scale (time-frequency) grid. This visualization, called the scalogram or mean square map, reveals the frequency content of the signal at each time step to pinpoint the occurrence of transients while tracking evolutionary phenomena in both time and frequency.

In some recent studies, the concept of the scalogram has been advanced to identify correlation between signals in which the squared coefficients are replaced with the product of the wavelet coefficients of two different processes (e.g., Gurley and Kareem 1999a). This coscalogram produces a view of the coincident events between the processes, revealing time-varying pockets of correlation over frequency.

To demonstrate this concept, full-scale pressures measured on a building and the upstream wind velocity fluctuations are analyzed. The scalogram of wind velocity and simultaneously measured pressure are presented along with their coscalogram in Figs. 1(a–c). The dark hues of the coscalogram identify areas of correlation. Figs. 1(d–f) present the same information for two uncorrelated records. The resulting coscalogram [Fig. 1(f)] of these two unrelated processes shows no distinct correlation. The coscalogram contains wavelet coefficients determined from segments of the signal isolated by the sliding window of the scaled parent wavelet. At each time step, the calculated wavelet coefficients comprise a single raw spectrum across the range of scales, equivalent to a spectrum obtained from a single time history in the traditional Fourier analysis. These raw spectra that are assembled along the time axis in the scalogram and coscalogram lack the ensemble averaging necessary in traditional Fourier methods to reduce the variance in the estimate, resulting in noisy displays where correlated events are difficult to differentiate from random coincident coefficients. Though this simple measure of correlation has been used to qualitatively identify first-order wind
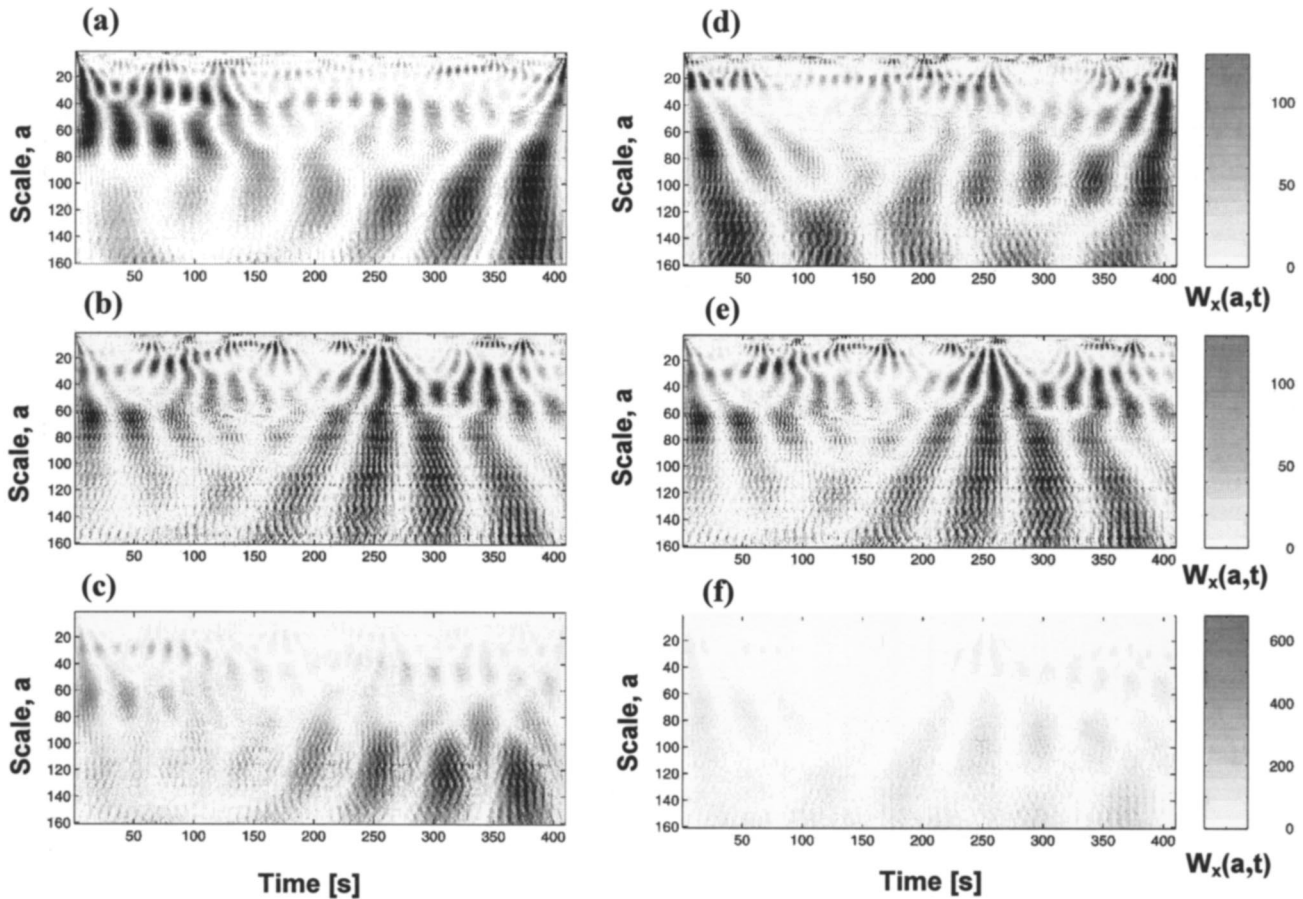
Fig. 1. (a) Scalogram of upstream wind velocity 1; (b) scalogram of rooftop pressure; (c) coscalogam of these two correlated processes; (d) scalogram of upstream wind velocity 2; (e) scalogram of rooftop pressure; and (f) coscalogram of these two uncorrelated processes

velocity and pressure relationships (Gurley and Kareem 1999a), it is refined in this study by the introduction of a wavelet coherence measure.

It should be noted that other studies have applied higher-order spectral analysis to quantify the nonlinear relationship between wind velocity and pressure (Gurley et al. 1997). However, these Fourier-based higher-order spectral methods are not capable of capturing the transient intermittent relationship being sought here. A more accurate and reliable approach to quantitatively identify intermittent first- and higher-order correlation is the thrust of this study.

Wavelet-Based Coherence Map

As the Morlet wavelet is merely a localized form of the Fourier transform, it can intuitively be substituted into classical spectral measures to uncover time-varying frequency content, effectively windowing the Fourier analysis. The equivalence of traditional Fourier measures with those newly recast using Morlet wavelets was previously shown in Gurley and Kareem (1999a) for quantities such as scalogram and coscalogram, analogs to the autospectrum and cross spectrum. In the current study, the classical coherence definition is modified utilizing spectra defined locally by Morlet wavelets to yield a time-frequency coherence function. The traditional form of the coherence function can be retained as the ratio of the wavelet cross spectrum to the product of the

wavelet autospectra of the two signals $x(t)$ and $y(t)$. The wavelet coherence map is thus defined as

$$[c^W(a,t)]^2 = \frac{|S^W_{xy}(a,t)|^2}{S^W_{xx}(a,t)S^W_{yy}(a,t)} \tag{4}$$

where the localized power spectra discussed above are given by

$$S^W_{ij}(a,t) = \int_T W^*_i(a,t)W_j(a,t)d\tau \tag{5}$$

The localized time integration window in Eq. (5), $T=[t-\Delta T,t+\Delta T]$, is selected based on the time resolution desired in the resulting coherence map and essentially performs the same ensemble averaging operation, albeit localized in time, as traditional Fourier analysis to obtain an auto-spectrum or cross spectrum of two signals. The map is bounded between 0 and 1 and provides a view of the localized correlation with respect to both time and frequency. An equivalence of this proposed time-frequency coherence map with its classical formulation is demonstrated in the following section.

It should be noted that discussions in Torrence and Compo (1998) highlight that an earlier coherence measure defined by Liu (1994), similar to that used by Shin et al. (1999), had limited physical meaning without the smoothing introduced here by T in Eq. (5), and hint that averaging to some extent is necessary to provide a useful measure of coherence. The parameter T in Eq.
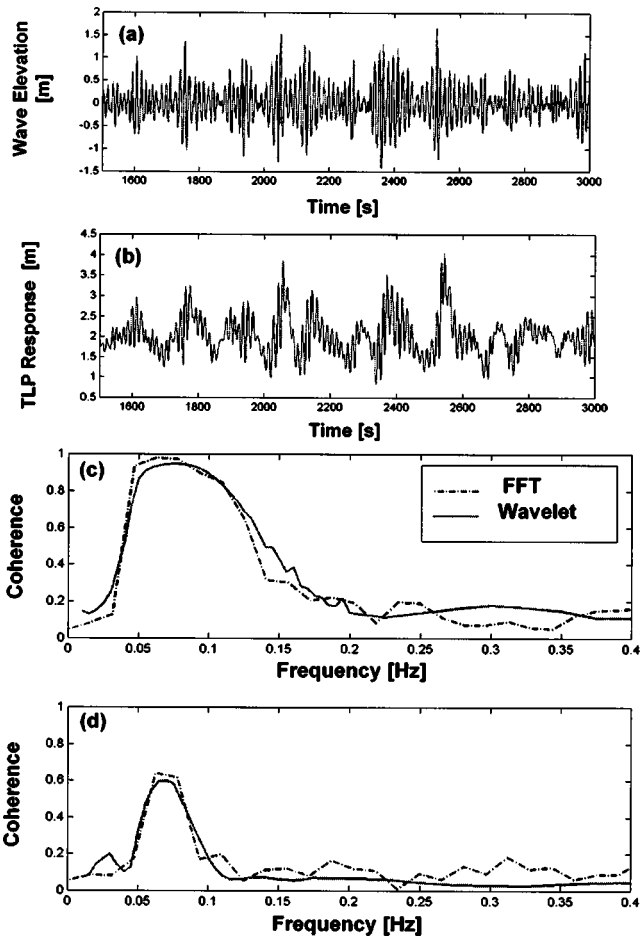
Fig. 2. (a) Incoming wave surface elevation; (b) tension leg offshore platform surge response; (c) wavelet and fast Fourier transform coherence estimates between wave elevation and tension leg offshore platform response; and (d) wavelet and FFT coherence estimates between wave elevation and tension leg offshore platform response with incoherent noise added to each

(5) addresses this concern, although, being somewhat arbitrary, it also presents the potential for a loss in time localization.

Comparison of Wavelet- and Fourier-Based Coherence Estimates

The validity of the coherence map in Eqs. (4) and (5) is demonstrated by first applying the wavelet-based coherence to stationary signals. The standard Fourier-based coherence estimate is directly compared with the wavelet-based coherence by averaging out the time information in the wavelet coherence map, according to

$$[c^W(a)]^2 = \frac{1}{nt} \sum_{i=1}^{nt} [c(a,t_i)]^2 \qquad (6)$$

where nt = number of discrete time steps resulting from the localized time window T.

The signals being analyzed in this example are the upstream wave elevation and the resulting surge response of a tension leg offshore platform (TLP) 1:200 scale model, measured experimentally in a wind/wave tank facility and shown in Figs. 2(a and b). Sampled at 1 Hz, 4,096 s of data is used in this analysis. Standard Fourier coherence estimation and Eqs. (4)–(6) are applied to these signals with the results shown in Fig. 2(c). The coherence is
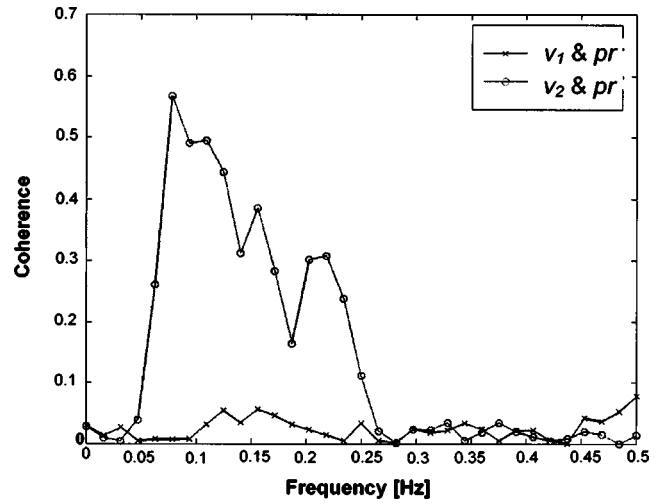

Fig. 3. Coherence between $v_2(t)$ and pr(t) and between $v_1(t)$ and pr(t)

well represented by both estimates, demonstrating the accuracy of the wavelet-based coherence estimate with respect to both magnitude and frequency. A second example demonstrates that wavelet-based coherence can accurately estimate smaller levels of linear correlation. In this case, independent white noise vectors are added to the wave surface and TLP response time histories to reduce the level of correlation, and coherence estimates are again produced. Fig. 2(d) shows the wavelet coherence representing the reduced correlation accurately.

Application of Wavelet-Coherence to Nonstationary Signals

The previous section demonstrated that wavelet-coherence viewed only with respect to frequency provides an effective coherence estimate. The advantage of wavelet-based coherence is now demonstrated by its application to velocity and pressure signals with known pockets of short duration correlation. Two independent Gaussian wind velocity signals $[v_1(t), v_2(t)]$ are simulated for 2,048 s at 1 Hz. A pressure record is then created by combining independent white noise $\varepsilon(t)$ with the $v_2(t)$ wind record

$$\text{pr}(t) = \varepsilon(t) + v_2(t) + G[\varepsilon(t)^2 + v_2(t)^2] \qquad (7)$$

For this example, $G = 0.05$. Two small segments of the pressure record, over the time interval t', are then replaced with signals generated by

$$\text{pr}(t') = \varepsilon(t') + v_{1f}(t') + G[\varepsilon(t')^2 + v_{1f}(t')^2] \qquad (8)$$

where $v_{1f}(t')$ indicates $v_1(t')$ after band-pass filtering is applied to correlate the pressure and the velocity record over selected frequency ranges. The use of Eq. (8) produces a pair of signals, pr(t) and $v_1(t)$, correlated only from 512 to 768 s between 0.0625 and 0.25 Hz and from 1,536 to 1,792 s between 0.19 and 0.37 Hz, and uncorrelated everywhere else.

The standard Fourier-based coherence between $v_2(t)$ and pr(t) and between $v_1(t)$ and pr(t) are displayed in Fig. 3. Note that the intermittent coherence between $v_1(t)$ and pr(t) cannot clearly be distinguished, suggesting that the signals are uncorrelated, whereas the relationship between $v_2(t)$ and pr(t), as expected, appears fairly strong.
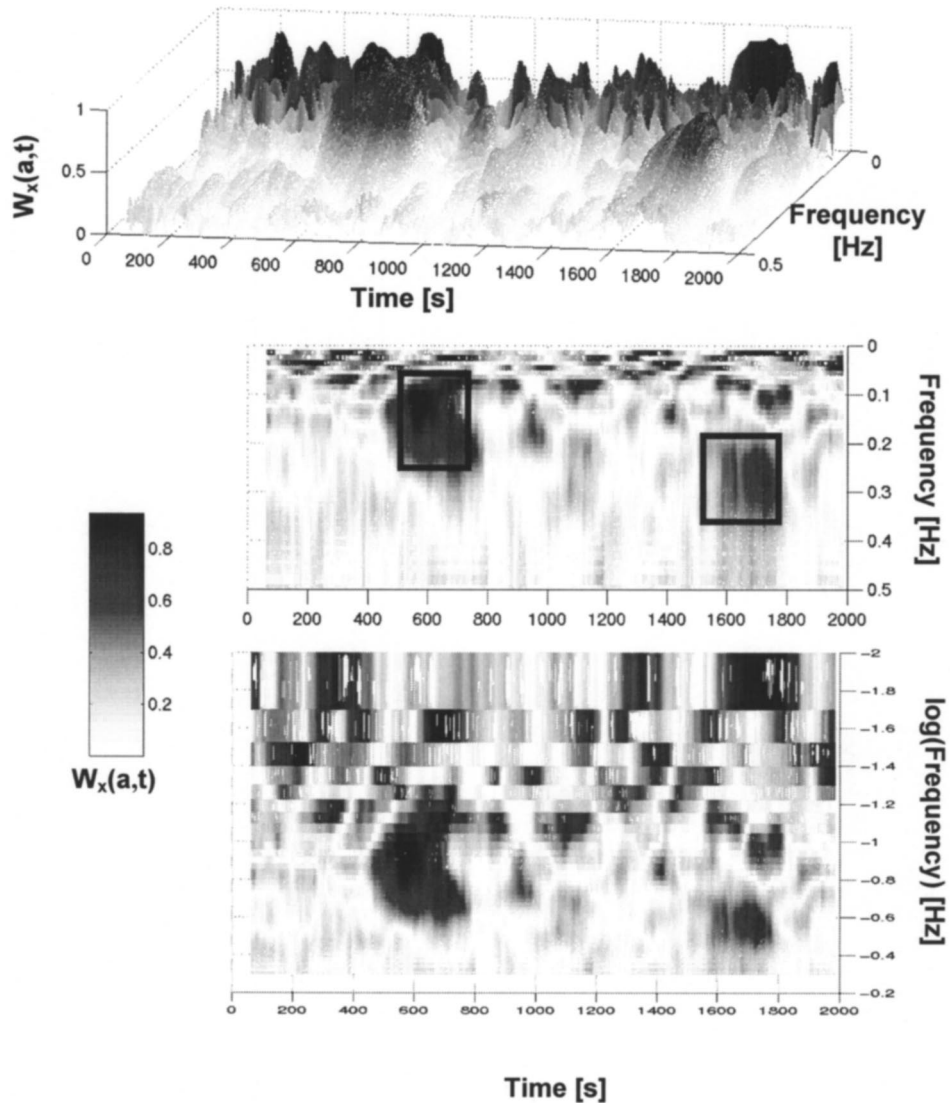
Fig. 4. Wavelet coherence map between $v_1(t)$ and $\mathrm{pr}(t)$, also shown as semilogarithmic in frequency, emphasizing low-frequency content

Isometric and overhead views of the wavelet-coherence map between $v_1(t)$ and $\mathrm{pr}(t)$, as generated by Eq. (4), are shown in Fig. 4. For this example, and those which follow, a value of $f_o = 5/(2\pi)$ was deemed sufficient to provide the necessary time and frequency resolutions, though a more precise frequency resolution (larger f_o) may be required in other cases, as discussed in Kijewski and Kareem (2002a). A time integration window of $T = [t - 64 \text{ s}, t + 64 \text{ s}]$ was applied. Pockets of strong correlation can be identified in these displays that include the time and frequency regions of introduced correlation, approximately boxed. However, the coherence estimate also displays phantom correlation in regions where no correlation exists, particularly in the low-frequency regions as emphasized by the semilogarithmic plot in Fig. 4. This noise is similar to that seen in Fourier-based spectral methods, where, due to a finite number of ensembles, variance errors are introduced. In the case of the wavelet coherence map, the localized time integration window T determines the number of ensembles used in the estimation of coherence in Eq. (4). Increasing T can reduce the noise in the coherence estimate at the expense of temporal.

Minimization of Spurious Coherence

Classically, the presence of variance in raw spectral estimates necessitates the use of averaging in order to obtain more reliable results. However, the transient information sought in a time-frequency analysis may be obscured through excessive averaging, especially in the low-frequency regime, where spurious coherence seems most prevalent. A variable integration scheme is proposed in the following section to address this issue, followed by alternative approaches designed to better preserve temporal resolution.

Multiresolution Integration Windows

In the initial formulation of the wavelet coherence, the localized time window is constant throughout the analysis. However, unlike its Fourier counterpart, the wavelet transform is multiresolution, having scale-dependent time and frequency resolutions. Each wavelet coefficient, at given (frequency) scale a_i and time t_j, is the result of analyzing a local section of the time history windowed by the scaled Gaussian function of the Morlet wavelet.
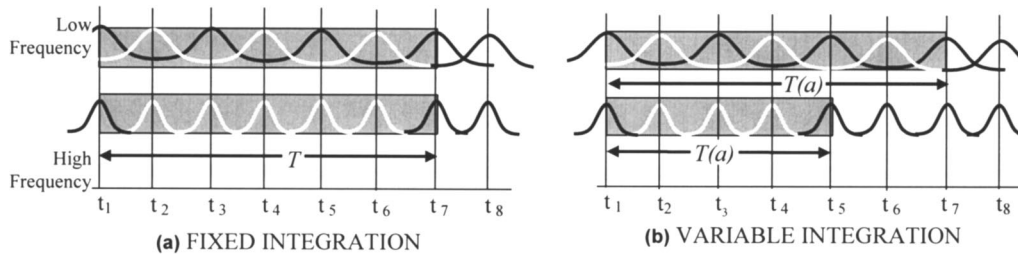
Fig. 5. Illustration of variable integration window concept

Thus, the signal's content Δt before that point in time and Δt after that point in time is used to estimate the wavelet coefficient $W_x(a_i, t_j)$, where Δt is dictated by a_i according to Eq. 3(*a*).

For the analysis conducted in the Section, "Application of Wavelet-Coherence to Nonstationary Signals" and shown in Fig. 4 (referred to herein as the baseline example), the choice of a constant window spanning a total of 128 s implies that at very low frequencies, as little as one unique local section of the time history is effectively being included in the estimate of the wavelet local spectrum in Eq. (5). For $f_o = 5/2\pi$, at 0.01 Hz nearly all the wavelet coefficients in that 128 s time span are estimated from the same section of the time history, approximately 112 s long ($\Delta t \sim 56.27$ s), and are thereby virtually nonunique. Thus, their subsequent averaging does little to reduce the variance, as conceptualized by Fig. 5(*a*). The figure illustrates that at low frequencies there can be considerable overlap of the Morlet wavelet's Gaussian window within the analysis horizon T, yielding only three unique wavelet windows, shown in white. Conversely, at higher frequencies, the same T affords five unique wavelet windows. The ramifications parallel the estimation of power spectra from Fourier-transformed blocks of a time history. Consider a signal of finite duration from which five raw spectra can be generated only by heavily overlapping the blocks of the time history being Fourier transformed. These five spectra are highly dependent and thus only minimally reduce the variance when averaged. However, if the signal were long enough to estimate five raw spectra from nonoverlapping segments of the signal, their averaged result would have far less variance, just as in the case of the higher frequencies in Fig. 4, whose wavelet coefficients are estimated using windows with temporal duration of only a few seconds. The localized spectra in Eq. (5) at these frequencies include markedly more wavelet coefficients generated from independent segments of the time history. Now the same $f_o = 5/2\pi$ Morlet wavelet, at 0.5 Hz, produces a wavelet coefficient from only 2.24 s of data ($\Delta t \sim 1.12$ s), affording over 50 coefficients from nonoverlapping segments of the 128 s analysis window for averaging and sizeable reductions in variance. This explains why lower frequencies in the coherence map seem to be heavily plagued by spurious coherence, as emphasized when the coherence map is plotted as semilogarithmic in frequency in Fig. 4.

The use of a fixed integration window in Eq. (5) actually provides differential treatment to the high-frequency components, in terms of the number of uniquely estimated wavelet coefficients included in the averaging process. Due to the multiresolution character of the wavelet analysis, T in Eq. (5) should be replaced by $T(a)$, so that the integration in Eq. (5) averages the same number of "ensembles" over all frequencies, as also conceptualized in Fig. 5(*b*). In this case, at both high and low frequencies there are at least three unique wavelet windows, shown in white.

The variable integration scheme proceeds by defining the window of integration for each frequency as an integer multiple (β)

of the temporal resolution of the analyzing wavelet at that scale, given as

$$T(a) \geqslant 2\beta\Delta t = \frac{2\beta a}{\sqrt{2}} = \frac{2\beta f_o}{f\sqrt{2}} \qquad (9)$$

for the Morlet wavelet. Thus, β would be chosen as a constant for the entire map, dependent on the number of desired averages in the coherence measure, and $T(a)$ would vary, inversely proportional to the frequency being analyzed. The inequality in Eq. (9) arises from the fact that the times at which the signal is sampled will not coincide with the effective initiation and termination of an arbitrary dilated wavelet, such that $T(a)$ must be rounded to the nearest sampled point. This fact leads to the overlapping which may occur at lower frequencies, as visualized in Fig. 5. Note that Eq. (9) insures that there is a minimum of β independent time segments being windowed in the estimation of wavelet coefficients, but there certainly may be additional overlapping ensembles present, especially in the lower frequencies. As the number of independent ensembles makes the most significant contributions to variance reduction, it allows the simplest and most direct criteria for defining $T(a)$.

In Fig. 6, the benefits of variable integration are evaluated by comparing the baseline case to three other cases: $\beta = 10$, 20, and 50. Note that in the baseline case, the fixed integration window yielded approximately $\beta = 50$ in the high frequencies while affording as little as $\beta = 1$ in the low frequencies, accounting for the prevalence of spurious coherence in this region. As shown in Fig. 6, by averaging over a horizon long enough to permit a sufficient number of wavelet coefficients to be estimated from nonoverlapping windowed sections of the time history, much of the low-frequency spurious coherence is minimized. The higher frequencies still appear to be plagued in comparison to the baseline case, as expected, since the baseline essentially had $\beta = 50$ in this region. Increasing the number of ensembles being averaged to $\beta = 20$ and 50 yields further improvements in the higher frequencies, though the known pockets of coherence are now beginning to bleed temporally, a consequence of increasing the time frame for local averaging. This loss of temporal resolution in the coherence map is an unavoidable consequence of increasing the number of ensembles in the averaging process. However, the examples provided in Fig. 6 illustrate that meaningless coherence can be attributed to the effective number of ensembles in the averaging process in Eq. (5) and justifies the use of a variable time window for this integration, as defined by Eq. (9). Unfortunately, the loss of temporal accuracy places practical limits on the use of localized integration to diminish spurious coherence, motivating more sophisticated techniques to remove noise from the map.
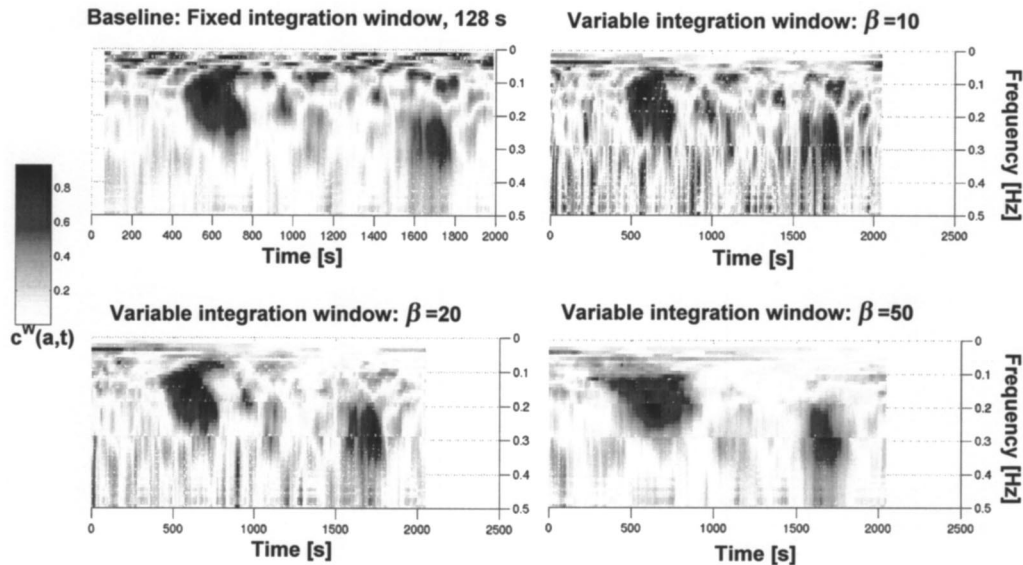
Fig. 6. Examples of variance reduction by variable integration window

Ridge Extraction by Hard Thresholding

As wavelet analysis is used commonly for the study of evolutionary behavior with relatively short duration data, the possibility of significant amounts of averaging becomes increasingly difficult if not impossible, particularly if the signal contains transient information that would be completely obscured in the averaging process. An alternative approach is to separate the signal from the noise surrounding it. In the case of analyzing wavelets whose Fourier transforms are sharply focused near a fixed frequency value (e.g., Morlet wavelet), the maxima of the resulting wavelet transform reflect the locations where the energy of the signal concentrates, defining a curve in the time-frequency plane termed the ridge—quite useful in situations where frequency-modulated signals are imbedded in noise. Although noise is spread throughout the time-frequency plane, the contribution of the signal is much greater than the noise in the vicinity of the ridges. Exploiting this, the signal ridges may be identified through simple algorithms that seek out the local maxima of the modulus of the transform at each instant in time. More sophisticated approaches that utilize known properties of the ridge can be applied when noise is more prevalent (Carmona et al. 1998).

However, in the coherence analysis presented here, the coherent pockets are intermittent and not suitable for extraction techniques geared for smooth, continuous ridges. Still, the theory of ridges implies that globally, the truly coherent pockets will show stronger coherence than the surrounding noise. As a result, the truly coherent pockets may be separated by globally identifying the maximum coherence ($\max[c^w]$) in the map and applying denoising schemes such as hard thresholding (Gurley and Kareem 1999a)

$$c^{W,\mathrm{hard}}(a,t) = \begin{cases} 0 & \text{if} \quad c^w(a,t) < \lambda \max[c^w] \\ c^w(a,t) & \text{if} \quad c^w(a,t) \geq \lambda \max[c^w] \end{cases} \quad (10)$$

This process roughly approximates a ridge identification procedure, effectively extracting the locations where the true coherence lies. λ is the assigned threshold factor, taking on a value between 0 and 1 to define the percentage of the maximum coherence deemed meaningful. The thresholding not only removes spu-

rious coherence as the result of variance, but also removes the effects of the Gaussian windowing operation in the Morlet wavelet transform, which introduces a known level of leakage in the time and frequency domain, respectively, embodied by end effects and an increase in spectral bandwidth (Kijewski and Kareem 2002b). Though lesser values of coherence surrounding a point in time and frequency are produced as a result of this window, the highest coherences will still manifest along these ridge points, which carry all the meaningful coherence information.

The thresholding operation in Eq. (10) was applied to some of the cases considered in the previous section. The combination of ridge extraction by hard thresholding and variable integration provides a simple means to extract meaningful coherence from the wavelet coherence map. For $\beta = 10$, increasing the threshold factor to 0.75 approximately isolates both pockets of known coherence, as clearly shown when comparing the results from Fig. 6 to the filtered results in Fig. 7. However, by selecting too stringent a threshold ($\lambda = 0.90$, not shown), only a portion of the first pocket of coherence is retained, while the second is completely lost. When the number of ensembles is more sizeable, the threshold factor can be relaxed considerably, as $\beta = 50$, $\lambda = 0.50$ illustrates. Recall that this thresholding approach is merely another strategy to separate true coherence from noise. As the noise is primarily the byproduct of variance, or a lack of averaging, in cases where variable integration has insured a large number of ensembles in the average (e.g., $\beta = 50$), the noise has already been considerably alleviated (see Fig. 6). In such cases, the noise is less dominant, taking on lower amplitudes in comparison to the coherent ridges, thereby relaxing the necessary threshold value λ. Note again, that the bleeding of temporal information, particularly for the first pocket of known coherence, is an unavoidable consequence of increasing the number of ensembles in the averaging process. Thus far, the sections, ''Multiresolution Integration Windows'' and ''Ridge Extraction by Hand Thresholding'' have discussed two techniques for reducing the appearance of spurious wavelet coherence that, while simple, are quite subjective. The following
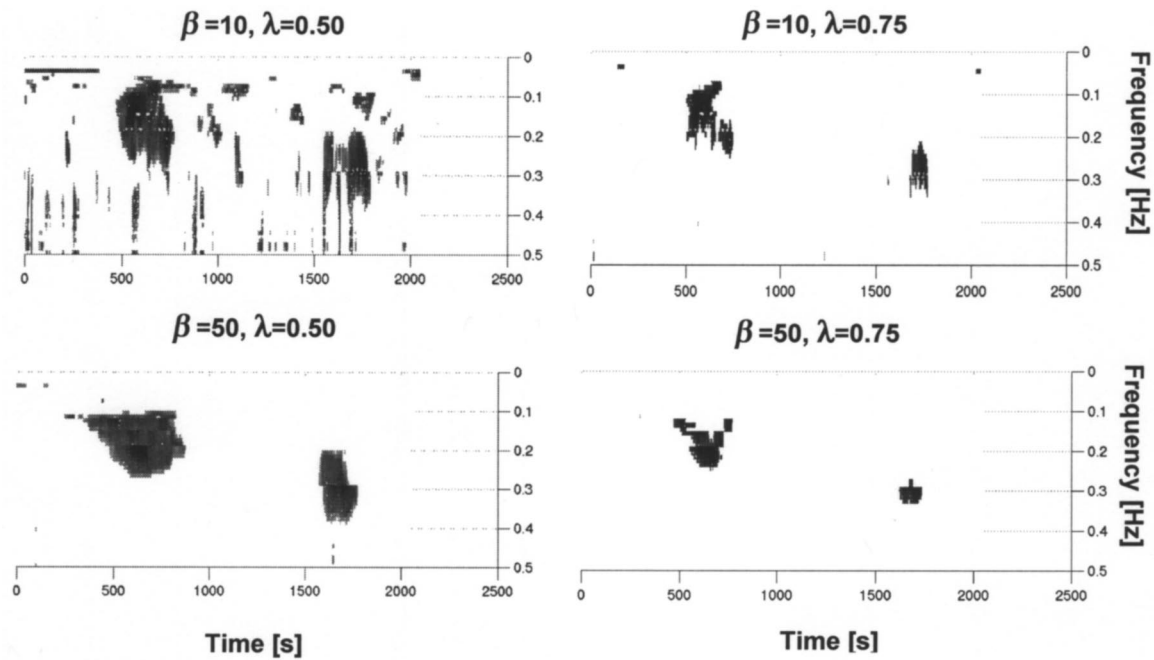
Fig. 7. Examples of coarse ridge extraction by thresholding

section discusses a more sophisticated technique that removes much of this subjectivity and provides an effective means to separate meaningful pockets of coherence.

"Smart" Ridge Extraction: Filtered Wavelet Coherence Map

Though the coarse ridge extraction by thresholding is a simple means to identify meaningful coherence, the insouciant use of hard thresholding based on global maxima may obscure meaningful coherence that is weaker than the dominant coherent components. Any coherence, real or noise induced, falling below the threshold value is neglected. Recognizing that the spurious coherence is the result of inherent randomness, one alternative would be to conduct repeated Monte Carlo simulations of white or colored random noise in order to determine the likely levels of variance in a given wavelet spectral measure. By this approach, peaks in a wavelet scalogram, for example, are deemed statistically significant if they surpass a given confidence level defined by the random noise simulations, as detailed in Torrence and Compo (1998). However, this technique is quite generalized and does not incorporate any specific information on the spectral or probabilistic structure of the analyzed signals. This was enhanced by Dunyak et al. (1997), who presented a method to quantify the statistical relevance of wavelet coefficients when detecting coherent wind gusts. These sustained gusts are delineated from short incoherent bursts by establishing a reference distribution of wavelet coefficients from simulated Gaussian signals with no sustained gusts. This notion can be extended for the purposes of wavelet coherence analysis by employing a "smart" thresholding scheme that exploits both the spectral and probabilistic information from the signals being analyzed to generate a map describing the expected noise threshold for a given pair of signals, $x(t)$ and $y(t)$ (Gurley and Kareem 1999b).

The expected noise map is developed by first generating multiple simulations of the second signal, denoted $y_s(t)$. These simulated signals are independent of each other and $x(t)$ and are statistically identical to the original signal $y(t)$ in both the power spectral density (PSD) and probability-density function (PDF), through the use of a recently developed non-Gaussian simulation algorithm (Gurley and Kareem 1997a).

The wavelet coherence between $x(t)$ and $y_s(t)$, delineated $[c_i^{nc}(a,t)]^2$, is then calculated for each of the N independent simulations, according to Eqs. (4) and (5). These coherence maps, which should contain no meaningful coherence and only embody coherence introduced by noise or leakage in the transform, are then averaged to produce a mean noise reference map

$$[c_{mn}(a,t)]^2 = \frac{1}{N}\sum_{i=1}^{N}[c_i^{nc}(a,t)]^2 \qquad (11)$$

with standard deviation $c_{st}(a,t)$. The threshold value of a statistically meaningful correlation can them be defined as the sum of this mean and the standard deviation weighted by a factor g

$$c_{th}(a,t) = c_{mn}(a,t) + g[c_{st}(a,t)] \qquad (12)$$

The factor g is selected based on the desired probability of exceeding the noise threshold. With the reference map $c_{th}(a,t)$ now in place, the actual coherence of $x(t)$ and $y(t)$ can be generated by Eq. (4) and then subjected to a "smart" thresholding scheme, yielding a filtered coherence map according to

$$c_F^W(a,t) = \begin{cases} 0 & \text{if} \quad c^W(a,t) < c_{th}(a,t) \\ c^W(a,t) & \text{if} \quad c^W(a,t) > c_{th}(a,t) \end{cases} \qquad (13)$$

The noise factor g in Eq. (12) must be selected judiciously, as a choice that is too large may negate statistically meaningful, albeit reduced, levels of correlation, as observed in the thresholding procedure in the previous section. While the choice of g may be rather arbitrarily defined, e.g., Hangan et al. (2001), a less subjective choice for g may be determined based on the probability distribution of the noise coherence maps.

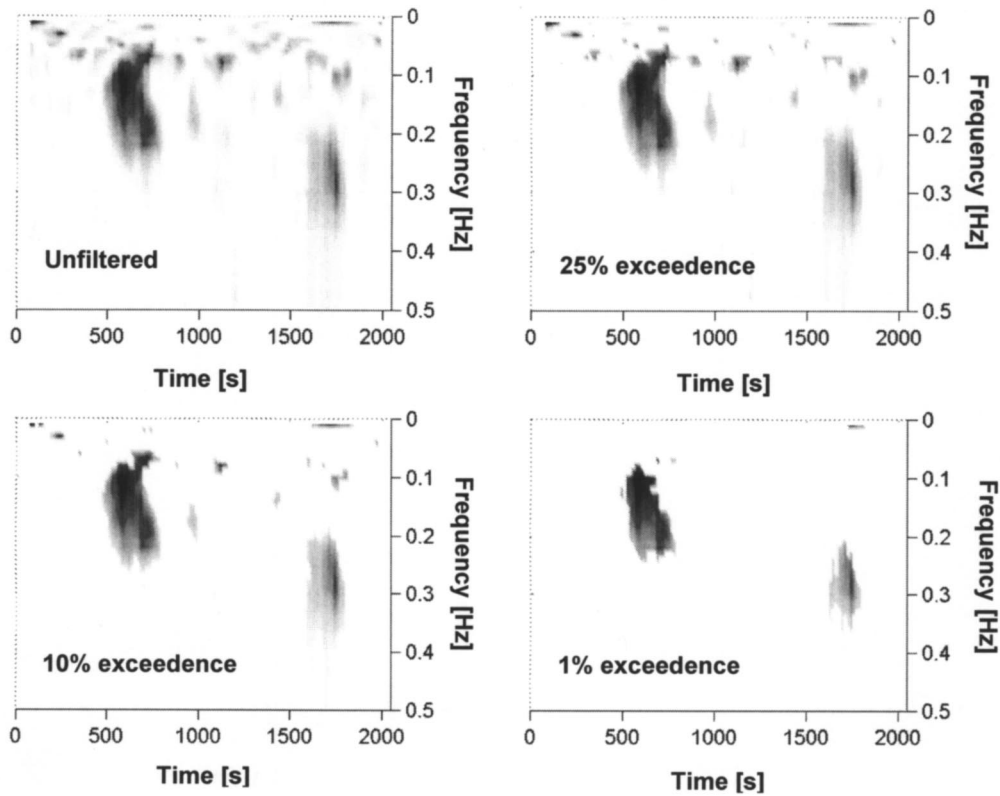The non-Gaussian probability distribution of the random noise

Fig. 8. Filtered wavelet coherence map between $v_1(t)$ and $\mathrm{pr}(t)$ with g selected for varying noise exceedence levels

map is approximated by considering higher-order statistics collected from the multiple simulated noise maps, in addition to their mean and standard deviation. As the extreme regions of the established distribution are used to determine the threshold, the probability model used must reliably reflect the actual distribution of noise. An extreme value-type distribution that does not explicitly include any information on the higher-order statistics is disregarded in favor of more advanced four parameter models. A modified Hermite polynomial-based model and a maximum entropy-based model are used for this study: Both of these have been shown to be very effective in representing the tail region of non-Gaussian processes (Gurely and Kareem 1997b) and produced almost identical results for the examples used in this study. The tail region of the resulting PDF represents the probability of noise exceeding the selected threshold that demarcates correlation in the wavelet coherence map. The noise factor g, in Eq. (12), is then selected based on the desired likelihood of noise exceeding the threshold, providing a quantitative measure of statistically meaningful correlation.

To illustrate the proper selection of the factor g, as well as the robustness of this approach, a filtered wavelet coherence map is generated using $N=100$ for the baseline analysis of the velocity and pressure signals, $v_1(t)$ and $\mathrm{pr}(t)$, discussed in the section, "Application of Wavelet-Coherence to Nonstationary Signals." Note that this baseline case does not exploit the use of the variable integration windows (see the section, "Multiresolution Integration Windows") and thus provides significant low-frequency noise. As Fig. 8 illustrates, the performance of the unfiltered map is greatly enhanced as the noise exceedence criteria is made more stringent. At the 1% exceedence level, both regions of known coherence are completely isolated, even in the low-frequency range, indicating that the technique cannot only remove spurious

coherence which results from variance, but also removes the window effects discussed previously that lead to leakage in the time-frequency plane.

To further illustrate the application of the filtered wavelet coherence map, measured full-scale incident wind velocity fluctuations and their corresponding pressure variation over a building surface are analyzed. Note the strong low-frequency correlation evident in the time histories of velocity and pressure shown in Figs. 9(a and b). The filtered wavelet coherence map is generated using a threshold reference map based on 500 simulated realizations of the data. Figs. 9(c–f) show the resulting filtered wavelet coherence map at several levels of the noise factor g. Extraneous noise again is removed as g increases, leaving a clearer portrait of the pockets of strong correlation. Though relatively intensive, the application of these filtered wavelet coherence estimates to wind data may be useful for identifying intermittent variations in the relationship between the velocity and pressure introduced by a change in wind direction or due to the evolution of a flow structure under the separation zone. Such maps can enhance the understanding of complex wind-structure interactions and open new avenues for data analysis, modeling, and simulation.

Scale/Frequency-Averaged Wavelet Coherence Map

Traditionally, coherence is displayed as a function of frequency only, averaged over the entire time duration, as shown previously in Fig. 3. As a result of the dual character of wavelet transforms, the resulting coherence maps may be manipulated in order to view coherence with respect to time. The wavelet coherence between two signals and those between the first signal and simulated versions of the second signal are each averaged over the scale component. In doing so, a display of the scale-averaged
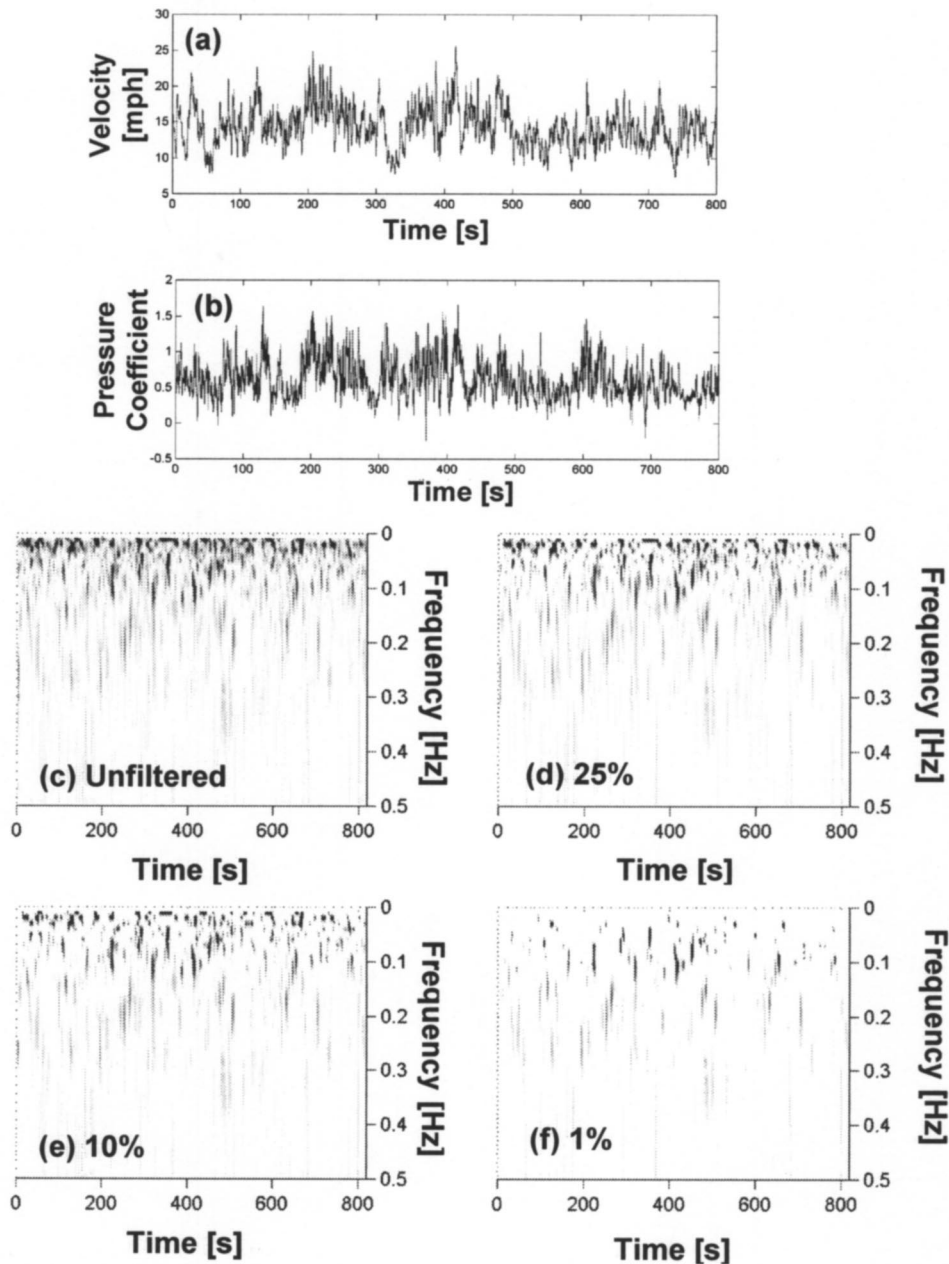
Fig. 9. (a) Measured wind velocity; (b) measured wind pressure; (c) unfiltered wavelet coherence map; filtered wavelet coherence map with *g* selected for varying levels of noise exceedence; (d) 25% exceedence; (e) 10% exceedence; and (f) 1% exceedence
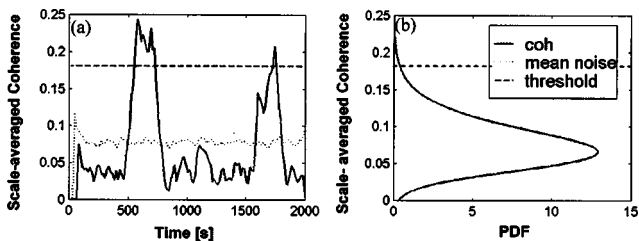

Fig. 10. (a) Scale-averaged coherence along with mean coherence and noise threshold and (b) Hermite polynomial-based probability density function model of reference noise maps

coherence, $\bar{c}(t)$, mean noise reference coherence, $\bar{c}_{mn}(t)$, and threshold coherence, $\bar{c}_{th}(t)$, between the two signals can be generated with respect to time rather than frequency. Such an interpretation for the simulated velocity and pressure $v_1(t)$ and $pr(t)$ is displayed in Fig. 10(a). The intermittent correlated regions clearly stand out as those surpassing the noise threshold, determined as a percent exceedence in the Hermite polynomial-based probability distribution model derived from the first four moments of the noise coherence maps as shown in Fig. 10(b).

Higher-Order Coherence

The wavelet coherence has been demonstrated to be useful for detecting localized linear coherent structures in time and frequency. However, higher-order spectral analysis must be con-

sulted for estimating nonlinear correlation, such as the use of bicoherence for second-order correlation (e.g., Nikias and Petropulu 1993; Gurley et al. 1997). The bicoherence is the ratio of the higher-order cross bispectrum to the first-order spectra. Due to its direct analogs to the Fourier transform, a Morlet wavelet transform may again be substituted in the bicoherence calculations to provide a time-frequency higher-order spectral equivalent.

One disadvantage of higher-order spectral techniques is the quantity of data needed to acceptably minimize variance errors in the higher-order spectral estimates. As a result, intermittent bursts of strong second-order correlation cannot be identified by applying a Fourier-based method over short time intervals without the benefit of additional variance reduction schemes. By extending the wavelet-based spectral estimation of coherence to the bicoherence estimates, the notion of a filtered wavelet bicoherence map can similarly be developed. Thus, the localized Fourier analysis that was once precluded is now made possible through this multiresolution wavelet framework to detect transient second-order relationships between two signals.

Wavelet Bicoherence

In this framework, wavelet coefficients are used to estimate bicoherence over short time intervals and are displayed with respect to both time and frequency. The time-scale wavelet cross bispectrum, given by

$$B_{xxy}^W(a_1,a_2,t) = \int_T W_x(a_1,\tau) W_x(a_2,\tau) W_y(a,\tau) d\tau \quad (14)$$

where

$$\frac{1}{a} = \frac{1}{a_1} + \frac{1}{a_2} \quad (15)$$

is used in the evaluation of the wavelet bicoherence (Powers et al. 1997; Gurley and Kareem 1999b)

$$[b_{xxy}^W(a_1,a_2,t)]^2 = \frac{|B_{xxy}^W(a_1,a_2,t)|^2}{\int_T |W_x(a_1,\tau) W_x(a_2,\tau)|^2 d\tau \int_T |W_y(a,\tau)|^2 d\tau} \quad (16)$$

Note that the wavelet coefficients simply replace the Fourier coefficients in the standard bicoherence, and integrals replace the expected value operator. The integration over short time windows in Eq. (16) provides an expectation over short time intervals. As currently defined, this local window T is fixed in duration over all frequencies, implying that this ensemble averaging is again differential over the range of frequencies. While the concept of variable integration can also be used to provide equal levels of variance reduction over all scales, the introduction of a filtered noise reference map was shown in the case of wavelet coherence to independently remedy the problem of spurious coherence. As a result of this, and for the sake of brevity, only the use of a filtered map for the wavelet bicoherence is discussed here.

Filtered Wavelet Bicoherence Map

The wavelet bicoherence defined in Eq. (16) can manifest spurious spikes, particularly in the low frequencies, as also noted by Powers et al. (1997). As discussed previously and demonstrated in Fig. 4, spurious coherence and similarly bicoherence is the result of insufficient averaging to remove the randomness in the estimation. Thus, following the success of reference noise maps in the estimation of coherence in the section, " 'Smart' Ridge Extraction: Filtered Wavelet Coherence Map," the same concept

is extended to the bicoherence measure to eliminate such spurious artifacts. Reference wavelet bicoherence maps are created between the first signal $x(t)$ and multiple independent simulations of the second signal $y_s(t)$, statistically identical to $y(t)$ in both PSD and PDF. The wavelet bicoherence maps between first signal and the simulations of the second signal are then averaged to produce a mean noise reference map, $b_{xxy}^{Wmn}(a_1,a_2,t)$. The standard deviation of the reference maps, $b_{xxy}^{Wst}(a_1,a_2,t)$, is also calculated, as well as their skewness and kurtosis. The threshold value of a statistically meaningful correlation, $b_{xxy}^{Wth}(a_1,a_2,t)$, is then given by

$$b_{xxy}^{Wth}(a_1,a_2,t) = b_{xxy}^{Wmn}(a_1,a_2,t) + g[b_{xxy}^{Wst}(a_1,a_2,t)] \quad (17)$$

with the noise factor g again selected based on the desired probability of noise exceeding the noise threshold, as discussed in the section, " 'Smart' Ridge Extraction: Filtered Wavelet Coherence Map."

The wavelet bicoherence maps are then compared with the threshold bicoherence map calculated in Eq. (17) to produce a filtered coherence map by "smart" thresholding

$$b_F^W(a_1,a_2,t)$$
$$= \begin{cases} 0 & \text{if} \quad b_{xxy}^W(a_1,a_2,t) < b_{xxy}^{Wth}(a_1,a_2,t) \\ b_{xxy}^W(a_1,a_2,t) & \text{if} \quad b_{xxy}^W(a_1,a_2,t) > b_{xxy}^{Wth}(a_1,a_2,t) \end{cases}$$
$$(18)$$

Application of Wavelet-Bicoherence to Nonstationary Signals

Validation of the proposed methodology is conducted by generating velocity and pressure signals with known pockets of short duration second-order correlation. Two independent wind velocity signals $[v_1(t),v_2(t)]$ are first created, each 4,096 s long, sampled at 1 Hz. The pressure record is created in the same way as detailed in the section, "Application of Wavelet-Coherence to Nonstationary Signals" using Eqs. (7) and (8), with the nonlinear term $G = 0.1$. The correlated time segments t' in Eq. (8) span time ranges from 1,000 to 1,600 s and from 3,000 to 3,400 s.

Eq. (16) is then applied to determine the bicoherence between $v_1(t)$ and $pr(t)$ over 16 equispaced segments spanning the entire time duration of the signals. This results in 16 bicoherence maps, each for a localized time span. Four of these maps are shown in Fig. 11(a), with their respective time region labeled. The first two figures in Fig. 11(a) display bicoherence measurements from the regions known to contain second-order correlation. The latter two figures display bicoherence measurements from regions known to have no correlation. As true of the coherence estimates in the section, "Wavelet-Based Coherence Map," these raw estimates contain noise, making identification of correlation difficult; however, implementation of the noise reference maps, as described in Eq. (18), permits true correlation to be distinguished from likely statistical noise. This is shown in Fig. 11(b), which displays the same four regions after filtering is applied. In this case, g was selected such that the probability of noise exceeding the threshold is 10%, and 1,000 independently simulated pressure records were used to generate the threshold reference map. The correlated time frames are clearly seen in the first two views of Fig. 11(b), while most extraneous noise was filtered out in the latter two uncorrelated segments.
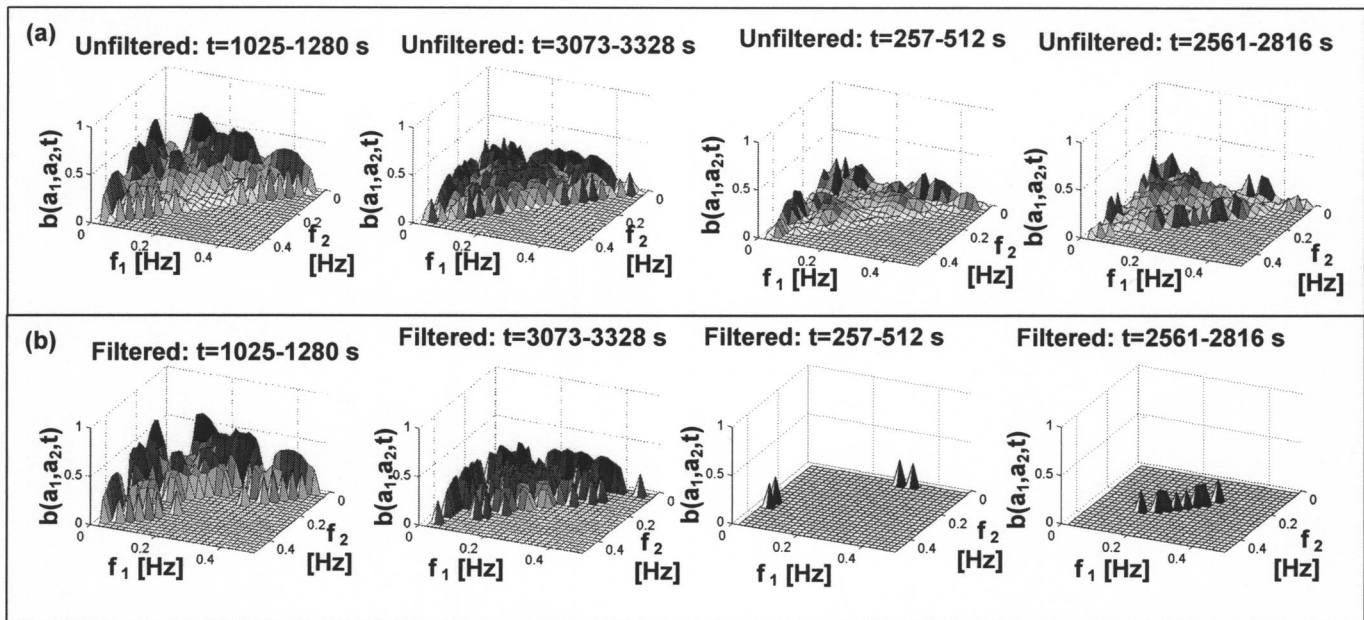
Fig. 11. Wavelet bicoherence maps between $v_1(t)$ and $pr(t)$: (a) unfiltered and (b) filtered. Signals are correlated over 1,025–1,280 s and 3,073–3,328 s, uncorrelated over 257–512 s and 2,561–2,816 s

Scale/Frequency-Averaged Wavelet Bicoherence Map

The multiple three-dimensional bicoherence maps shown in Fig. 11 can be reduced to a two-dimensional representation of second-order correlation by averaging the bicoherence over all scales for each time segment, according to

$$b_{xxy}^W(t) = \frac{1}{nf^2} \sum_{i}^{nf} \sum_{j}^{nf} b_{xxy}^W(f_i, f_j, t) \tag{19}$$

Application of Eq. (19) to the wavelet bicoherence maps previously generated reduces the 16 individual maps to 16 data points, shown in Fig. 12. This reduction is also applied to generate frequency-averaged mean reference bicoherence maps and their standard deviation to produce the threshold also shown in Fig. 12. Clearly, the time segments with known correlation can be identi-
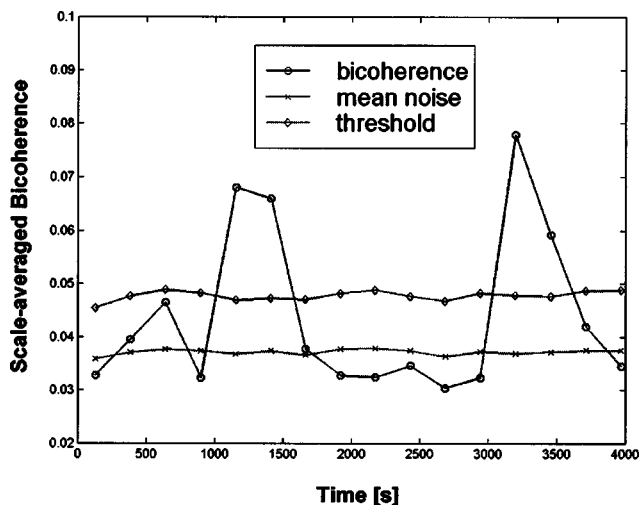

Fig. 12. Scale-averaged bicoherence of simulated velocity and pressure signals, $v_1(t)$ and $pr(t)$

fied as those exceeding the threshold level representing likely random noise. The frequency-averaged bicoherence provides only a qualitative display of the relative magnitude with respect to the noise threshold.

Bicoherence Example Using Measured Data

A second example illustrates the applicability of the wavelet bicoherence on measured experimental data. Recall the example presented in Fig. 2. The signals being analyzed are upstream wave elevation and the resulting surge response of a tension leg platform. Both viscous and inertial wave forces are acting on the platform, leading to strong first- and second-order correlation between the wave elevation and surge response throughout the time history (e.g., Tognarelli et al. 1997). In order to introduce regions where no correlation exists, two separate surge response records are combined. The wave elevation record $wv_1(t)$ and one of the response records $x_1(t)$ were measured simultaneously during the same experiment, while the second response record $x_2(t)$ was measured in a separate experiment, and thus uncorrelated with the wave elevation record $wv_1(t)$. For the total of 4,096 s of data, the following tailored response vector:

$$x(t) = [x_2(1-2{,}048) \quad x_1(2{,}049-2{,}560) \quad x_2(2{,}561-4{,}096)] \tag{20}$$

contains only one small time segment of data correlated with $wv_1(t)$ in the range of 2,049–2,560 s.

The wavelet bicoherence is again calculated over 16 equi-spaced time regions. Fig. 13(a) shows the unfiltered bicoherence estimates for two of these regions, with their respective time segments labeled, while Fig. 13(b) displays the improvement after filtering with a noise map. The time segment from 2,049–2,304 s represents a time frame where correlation exists, while the second time frame has no correlation. The spurious noise in this latter case is completely removed by the filtering procedure, while the former case is relatively unchanged, representing a region of meaningful correlation. The frequency-averaged bicoherence es-
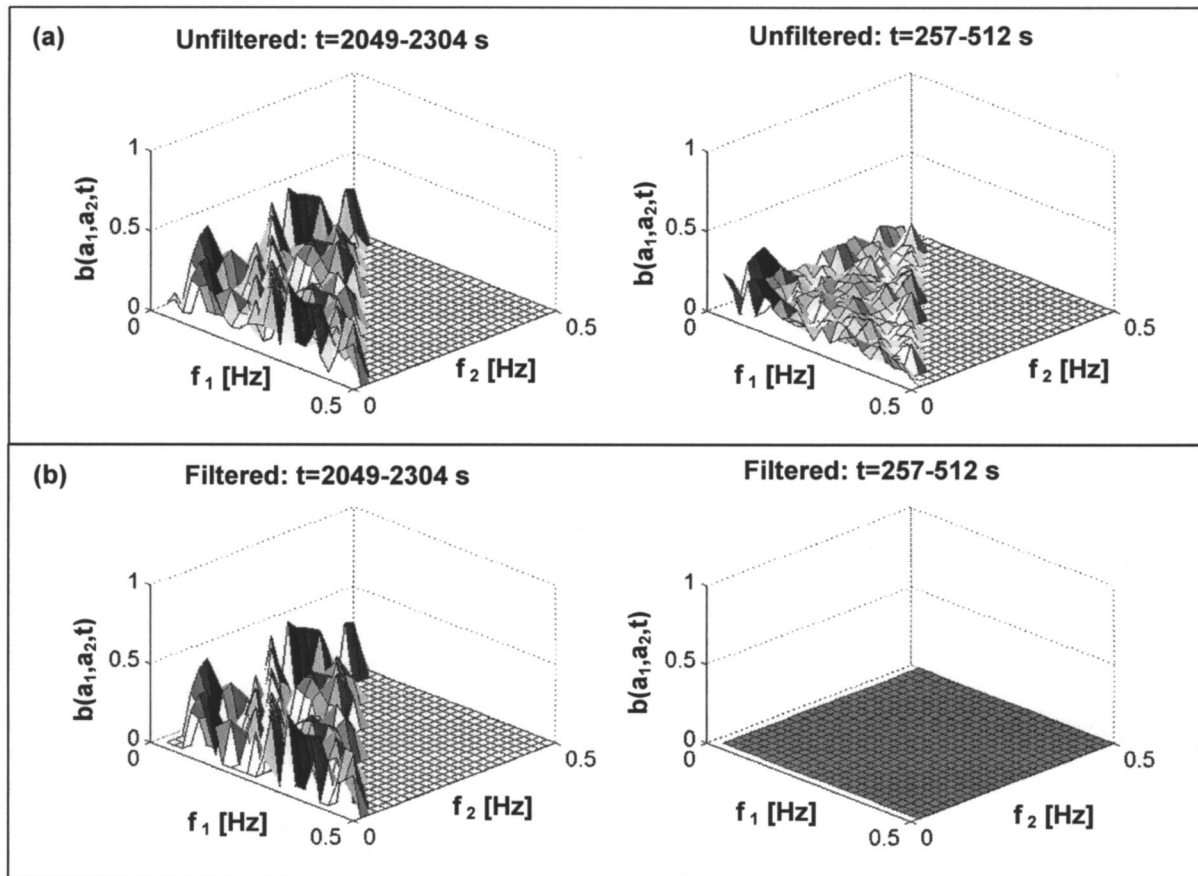
Fig. 13. (a) Unfiltered and (b) filtered bicoherence. $t = 2,049 – 2,304$ s represents correlated time segment, while $t = 257 – 512$ represents uncorrelated time segment

timate for each of the 16 time frames is shown in Fig. 14, identifying the known correlation region as the point at which the coherence exceeds the noise threshold. Both Figs. 13 and 14 clearly help in identifying the regions containing second-order correlation.
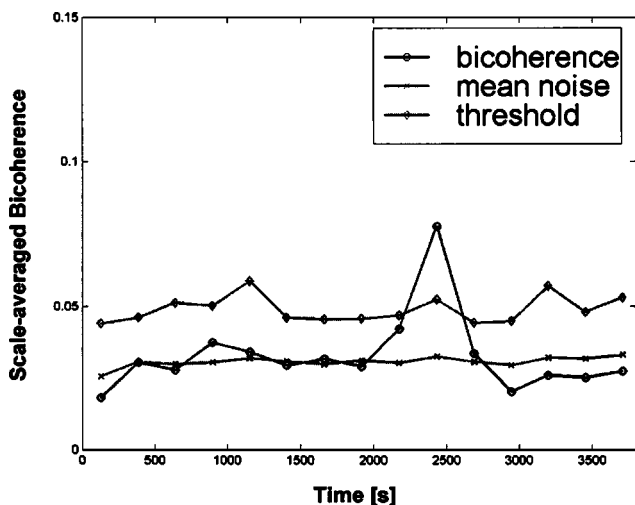

Fig. 14. Scale-averaged bicoherence of experimental tension leg offshore platform data

Conclusions

In this study, wavelet decomposition was used to produce a time-frequency display of the coherence and bicoherence between signals intermittently correlated. Unfortunately, raw spectral estimates used in the definition of coherence and bicoherence were inherently laden with statistical noise. The classical approach for reduction of variance is to perform ensemble averaging by using localized time integration. In this case, the introduction of a variable integration window was predicated on the multiresolution character of wavelets and highlighted that the lack of ensemble averaging results in much of the observed spurious coherence. Insuring sufficient ensembles in the average reduced the spurious coherence, though the loss of temporal resolution was a limiting factor. The theory of ridges was briefly introduced and the concept of hard thresholding based on global maxima of the wavelet coherence map was used as a coarse ridge extraction scheme to isolate meaningful coherence. The technique, when coupled with sufficient ensembles in the variable integration scheme, was shown to enhance performance. However, to preserve evolutionary characteristics while removing significant noise, more sophisticated approaches were required which do not involve extensive averaging. A "smart" thresholding simulation scheme was proposed to provide a reference noise map to separate spurious noise effects from true signal content. The noise was filtered from the display map by comparison with a threshold describing the likely noise level. This threshold was created by averaging a series of

reference correlation maps between one signal and uncorrelated simulations of the second signal. Examples demonstrated that this technique was capable of identifying both first- and second-order correlation and effectively reducing the presence of noise in the correlation displays for both simulated and measured data. Its robustness was further established as it was shown to alleviate the presence of spurious coherence, even in cases where variance and leakage were prevalent. Though relatively intensive, the proposed approach facilitated the removal of significant levels of all of the various contributing noise sources. In total, the wavelet-based first- and higher-order correlation detection analysis schemes presented here offer immediate applications where the determination of intermittent correlation between linear and nonlinear processes is required, e.g., bluff body aerodynamics in turbulent flows, wave-structure interactions in nonlinear random seas, and the nonlinear and nonstationary seismic response of structures.

Acknowledgments

References

Burrus, C. S., Gopinath, R. A., and Guo, H. (1998). *Introduction to wavelets and wavelet transforms: A primer*, Prentice-Hall, Englewood Cliffs, N.J.

Carmona, R., Hwang, W. L., and Torresani, B. (1998). *Practical time-frequency analysis*, Academic, San Diego.

Chui, C. K. (1992). *Wavelet analysis and applications: An introduction to wavelets*, Vol. 1, Academic, San Diego.

Daubechies, I. (1988). "Orthonormal basis of compactly supported wavelets." *Commun. Pure Appl. Math.,* 41, 909–96.

Daubechies, I. (1992). *Ten lectures on wavelets*, Society of Industrial and Applied Mathematics, Philadelphia.

Dunyak, J., Gilliam, X., Peterson, R., and Smith, D. (1997). "Coherent gust detection by wavelet transform." *Proc., 8th U.S. National Conference on Wind Engineering* (CD-ROM), Johns Hopkins Univ., Baltimore.

Farge, M. (1992). "Wavelet transforms and their applications to turbulence." *Annu. Rev. Fluid Mech.,* 24, 395–457.

Gabor, D. (1946). "Theory of communication." *Proc. IEEE,* 93(III), 429–457.

Grossman, A., and Morlet, J. (1985). "Decompositions of functions into wavelets of constant shape and related transforms." *Mathematics and physics, lecture on recent results*, L. Streit, ed., World Scientific, Singapore, 135–165.

Gurley, K., and Kareem, A. (1997a). "Analysis, interpretation, modeling and simulation of unsteady wind and pressure data." *J. Wind. Eng. Ind. Aerodyn.,* 69–71, 657–669.

Gurley, K., and Kareem, A. (1997b). "Modeling PDFs of non-Gaussian system response." *Proc., 7th Int. Conf. on Structural Safety and Reliability* (ICOSSAR), Kyoto, Japan.

Gurley, K., and Kareem, A. (1999a). "Application of wavelet transforms in earthquake, wind, and ocean engineering." *Eng. Struct.,* 21, 149–167.

Gurley, K., and Kareem, A. (1999b). "Higher order velocity/pressure correlation detection using wavelet transforms." *Wind engineering into the 21st Century, Proc., 10th Int. Conf. on Wind Engineering*, Copenhagen, Denmark, Vol. 1, Larsen, Larose and Livesey, eds., Balkema Press, Rotterdam, The Netherlands, 431–436.

Gurley, K., Tognarelli, M., and Kareem, A. (1997). "Analysis and simulation tools for wind engineering." *Probab. Eng. Mech.,* 12(1), 9–31.

Hangan, H., Kopp, G. A., Vernet, A., and Martinuzzi, R. (2001). "A wavelet pattern recognition technique for identifying flow structures in cylinder generated wakes." *J. Wind. Eng. Ind. Aerodyn.,* 89, 1001–1015.

Kijewski, T., and Kareem, A. (2002a). "Wavelet transforms for system identification: Considerations for civil engineering applications." *Comput.-Aided Civ. Infrastruct. Eng.*, in press.

Kijewski, T., and Kareem, A. (2002b). "On the presence of end effects and associated remedies for wavelet-based analysis." *J. Sound Vib.*, in press.

Liu, P. C. (1994). "Wavelet spectrum analysis and ocean wind waves." *Wavelets in geophysics*, E. Foufoula-Georgiou and P. Kumar, eds., Academic, San Diego, 151–166.

Mallat, S. (1998). *A wavelet tour of signal processing*, Academic, San Diego.

Nikias, C. L., and Petropulu, A. P. (1993). *Higher-order spectral analysis, a nonlinear signal processing framework*, PTR Prentice-Hall, Englewood Cliffs, N.J.

Powers, E. J., Park, S. I., Mehta, S., and Yi, E. J. (1997). "Higher-order statistics and extreme waves." *IEEE Signal Processing Workshop on Higher Order Statistics*, Alberta, Canada, 98–102.

Shin, Y. J., Powers, E. J., and Yi, E. J. (1999). "Comparison of time-frequency representations of random wave elevation data." *Proc., 9th Int. Offshore and Polar Engineering Conf.*, Brest, France, 34–40.

Strang, G., and Nguyen, T. (1996). *Wavelets and filter banks*, Wellesley-Cambridge Press, Wellesley, Mass.

Tognarelli, M., Zhao, J., Rao, K. B., and Kareem, A. (1997). "Equivalent statistical quadratization and cubicization for nonlinear systems." *J. Eng. Mech.,* 123(5), 512–523.

Torrence, C., and Compo, G. P. (1998). "A practical guide to wavelet analysis." *Bull. Am. Meteorol. Soc.,* 79, 61–78.